Fe and Co adatoms on bilayer borophene as single-atom catalysts for the oxygen-reduction reaction: A theoretical study

Walter Orellana[1,*] and Roberto H. Miwa[2]

[1]*Departamento de Ciencias Físicas, Facultad de Ciencias Exactas, Universidad Andres Bello, Sazié 2212, Santiago 837-0136, Chile*

[2]*Instituto de Físicas, Universidade Federal de Uberlândia, C.P. 593, Uberlândia, MG 38400-902, Brazil*

This study employs first-principles density-functional-theory (DFT) calculations and *ab initio* molecular dynamic (AIMD) simulations to investigate the stability, electronic properties, and oxygen-reduction reaction (ORR) activity of M adatoms ($M =$ Fe, Co) on free-standing bilayer borophene (BB) with different coverages. Our findings indicate that metals strongly bind to the BB surface, particularly at the hollow sites, inducing metallicity. We analyze the dissociation energy of O_2 and OOH after the adsorption on the metal center of BBM while ORR activity was assessed through the free-energy adsorption of their intermediates. The stability of the systems at electrochemical conditions was investigated by Pourbaix analysis as well as by AIMD simulations, which include explicit solvents. Our results suggest that BBCo in a low-coverage adatom configuration would exhibit competitive ORR activity, with a theoretical overpotential of around 1 V. However, this activity would only be feasible in alkaline environments where the stability BBCo is preserved. Hubbard-U corrections and the hybrid functional approaches within DFT are taken into consideration, and subsequent results are compared.

I. INTRODUCTION

Energy-conversion technologies like water electrolyzers, rechargeable metal-air batteries, and proton-exchange membrane fuel cells require high-performance catalysts to minimize reaction kinetic barriers of key processes like the oxygen-reduction reaction (ORR) [1–3]. The difficulties arise from the high energy needed to break O_2, of around 5 eV. Therefore, efficient electrocatalysts are required to lower the dissociation energy barrier for ORR. Currently, the most active ORR electrocatalysts are based on Pt and other precious metals, which are expensive and scarce [4,5]. Developments of low-cost and efficient ORR electrocatalysts are fundamental to improving the cost-effectiveness and large-scale commercial applications of emerging energy-conversion technologies.

Single-atom catalysts (SACs) with highly active sites, typically $3d$ transition metals dispersed on carbon substrates, have shown electrocatalytic activity for ORR [6–8]. From the pioneering work of Jasinski on the ORR activity of transition-metal phthalocyanines [9], a large number of studies on the subject have appeared [10–12], becoming the inspiration for alternative catalyst materials like FeN_4 centers embedded in graphene or graphitic carbon [3,13–21]. Fe/N/C-type catalysts have shown

promising performances for the reduction of O_2 [10,13] and CO_2 [22,23], close to those found on Pt-based catalysts. It is worth noticing that the energy barriers for O_2 dissociation on the highly reactive Pt(111) surface have been theoretically estimated between 0.6–0.9 eV [18,24–26]. Hence, the quest for suitable substrates that support selected transition metals, thereby reducing the surface work function and enhancing charge transfer, has emerged as a key issue in electrocatalysis. This is particularly significant due to the suggested link between work function and catalytic activity [27–30].

Boron atoms have a unique electronic structure that leads to various allotropes, including the two-dimensional (2D) phases known as borophene. Unlike carbon in graphene, the electron deficiency of boron results in complex bonding, giving rise to different structural phases. Monolayer borophene, the lightest 2D material known, has been synthesized on Ag(111) and Au(111) surfaces, under ultrahigh vacuum conditions, where boron was deposited in a highly controlled dose using electron-beam evaporation from a high-purity elemental source [31–33]. In addition, several polymorphs of bilayer borophene (BB) have been proposed through first-principles calculations [34–44]. Recently, BB structures have been synthesized on Ag(111) and Cu(111) substrates [45,46]. One of these structures is consistent with two covalently bonded AA-staking α-phase borophene layers with $P6/mmm$

*worellana@unab.cl

space-group symmetry, containing isolated hollow hexagons, which is characterized by an interlayer bonding density of $\nu = 1/4$ and a hollows density of $\eta = 1/12$ [42,47]. The presence of hollows in the triangular lattice leads to significant structural diversity for BB, which can be arranged in different patterns giving stability. This structure is predicted to be a 2D semiconducting material [42]. Further investigations pointed out not only the electronic properties of BB when compared with its monolayer counterpart but also the stability and mechanical properties in its free-standing form, mainly due to the interlayer covalent bonding [38,42,47], making it an interesting functional material. Indeed, suitable substrates for SACs require strong anchoring of the transition metal to prevent demetallation while preserving its electronic characteristics. In this respect, two-dimensional materials like graphene and borophene have emerged as promising substrates for SACs due to the lack of $3d$ electrons, avoiding interfering with the active site, namely the transition-metal atom [8]. Indeed, transition-metal-doped single-layer borophene has been theoretically explored as a single-atom catalyst for the nitrogen reduction to ammonia [48,49], and for the oxygen evolution reaction [50].

In this work, we study Fe and Co adatoms on free-standing bilayer borophene (BBFe and BBCo) as a single-atom catalyst for ORR, considering different adatom coverages. Our results reveal that both metal atoms strongly bind to the BB surface, preferentially at the center of the hollow hexagons, inducing metallicity and causing a decrease in the work function. Following the four-electron pathway, the ORR activity of BB and BBM systems is addressed by the free-energy adsorption of the elementary ORR intermediates (O, OH, and OOH). Further, the stability of BB and BBM in electrochemical conditions is analyzed by Pourbaix diagrams and by considering explicit solvents through AIMD simulations. Our results reveal that BBCo shows both stability in alkaline media and ORR activity comparable with those exhibited by Pt(111) and FeN$_4$ centers in graphene.

II. COMPUTATIONAL DETAILS

Spin-polarized density-functional-theory (DFT) calculations were performed using the Quantum Espresso *ab initio* package [51,52]. We used the Perdew-Burke-Ernzerhof (PBE) [53] generalized gradient approximation to describe the exchange-correlation potential, including van der Waals (vdW) interactions through the vdW DF functional [54]. In addition, for Fe and Co adatoms we include the Hubbard-U term ($U = 3.0$ eV) to account for the on-site Coulomb repulsion between $3d$ electrons (PBE+U), providing a more accurate description of the electronic correlations [55]. Norm-conserving pseudopotentials were used to describe the core-valence interaction [56], considering energy cutoffs of 60 and 480 Ry for wave
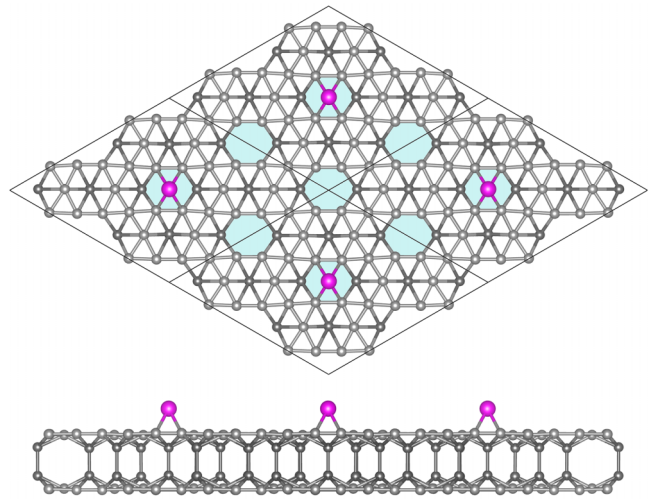

FIG. 1. Top and side views of the bilayer borophene structure for a metal-adatom coverage of $\theta = 1/4$. Gray and magenta balls represent boron and metal atoms. Dark-gray balls represent boron atoms forming interlayer B—B bonds, and the shaded areas indicate the hollow hexagons.

function and charge-density Fourier expansions, respectively. M adatom ($M =$ Fe, Co) on bilayer borophene was simulated with a hexagonal (4×4) surface unit cell, containing 88 atoms plus the M atom adsorbed on the hexagon hollow, as shown Fig. 1. We consider a vacuum region of 22 Å to ensure negligible interaction between images in the z direction. Brillouin-zone integration was performed using the $2 \times 2 \times 1$ Monkhorst-Pack k-point grid. All atoms were left free to relax until the residual force on each atomic component was less than 0.025 eV/Å.

Possible ORR activity of BBM was initially estimated by the O$_2$ and OOH adsorption energy on the metal center followed by the minimum energy path for their dissociation, using the climbing image nudged elastic band (NEB) formalism [57,58]. NEB is a minimum-energy-path search method between initial and final local minima allowing one to identify transition states or saddle points. This method optimizes several intermediate geometries (or images) along the reaction coordinate. Here, the O$_2$ and OOH dissociation energies were obtained by considering six intermediate images. Both side-on and end-on geometries were studied to find the equilibrium geometry of the adsorbed molecule on the metal (the initial local minimum). To find the equilibrium geometry of the dissociated molecule (the final local minimum), we explored different structures, looking for the most stable one. To establish a reference for the adsorption and dissociation energies of O$_2$ and OOH on BBM, we conducted calculations on the Pt(111) surface. This surface was represented by a (4×4) surface unit cell with four monolayers, where the bottom two layers were fixed in the bulk positions, considering a vacuum region of 15 Å. The Brillouin-zone sampling was performed with a $4 \times 4 \times 1$ Monkhorst-Pack k-point grid.

The other parameters were the same used throughout this work.

The ORR electrocatalytic activity of BB and BBM systems was assessed through the computational hydrogen electrode (CHE) model as proposed by Nørskov *et al.* [59]. This model relied on the adsorption strength of the ORR reaction intermediates OH*, O*, and OOH* on the catalyst's active site. The zero-point energy and entropic terms are determined by calculating the vibrational frequencies. Here, only the adsorbate vibrational modes are explicitly computed, while the substrate remains fixed. The entropy and vibrational frequencies of gasphase molecules are sourced from the NIST database. These calculations were performed with the Vienna *ab initio* simulation package (VASP), version 6.4.0, considering the projector augmented-wave method for the core-valence interaction [60], and a plane-wave cutoff energy of 500 eV. The exchange-correlation functional was modeled by the screened hybrid functional of Heyd-Scuseria-Ernzerhof (HSE06) [61,62], with 25% of exact exchange. The integration in the Brillouin zone was performed with the Γ point. The ORR activity of BB and BBM was also calculated using the PBE+U approach to evaluate its effectiveness.

The electrochemical stability of BB and BBM was examined in both acidic and alkaline environments through the generation of surface Pourbaix diagrams [63–66]. These diagrams serve as valuable tools to establish connections between the electrode potential and pH domains, providing insights into the thermodynamic stability of distinct phases under electrochemical conditions. Additionally, we assessed the stability of the systems considering explicit solutions through *ab initio* molecular dynamic (AIMD) simulations in specific alkaline and acidic environments. To achieve this, we constructed a periodic cell containing the BBM slab plus 64 H_2O molecules, adjusting the accessible volume to give the experimental density of water of 1 g/cm^3. The AIMD simulations were performed with the VASP code, employing the PBE exchange-correlation functional, including dispersion corrections due to the D3 method of Grimme *et al.* [67,68], other calculation parameters are the same as previously described. The simulations were performed in the canonical ensemble (NVT), using the Nosé-Hoover thermostat approach at 300 K, during 6 ps of simulation time, after 4 ps of stabilization, with a time step of 1 fs.

III. RESULTS AND DISCUSSION

A. Metal adatoms on bilayer borophene (BBM): Structural and electronic properties

The bilayer borophene surface has two symmetrically equivalent sites for metal adsorption, on the center of the hollow hexagons and on the center of the hexagon with interlayer B—B bonds at its center (see Fig. 1). We

calculate the binding energy of the metal atoms on these two sites, considering the (4×4) surface unit cell. We found an energetic preference for the hollow site with a gain in energy of 0.63 and 0.73 eV for BBFe and BBCo, respectively, where the metal adatom is projected 1.5 Å from the BB surface. Figure 1 shows the equilibrium geometry of BBFe with the Fe adatom adsorbed on the hollow site represented in the 4×4 surface unit cell. The stability of metal adatoms on BB was verified by the calculation of the binding energy (E_b), defined as

$$E_b = E_t(BBM) - E_t(BB) - E_t(M),$$

where $E_t(BBM)$ is the total energy of BB with a metal adatom; $E_t(BB)$ and $E_t(M)$ are the total energies of pristine BB and the isolated metal atom, respectively. Considering that BB has four hollow sites per (4×4) surface unit cell, we examine two metal-coverage configurations: a full coverage ($\theta = 1$), that is, four metal per unit cell, and a low coverage ($\theta = 1/4$), that is one metal per unit cell, where separation among Fe adatoms are 5.75 and 11.5 Å, respectively. Our results for the binding energy E_b and the equilibrium geometry of the M adatom on the hollow site for the two coverage under study are summarized in Table I.

The metal adsorption process for both coverages is exothermic, with a gain in energy higher than 3 eV for BBFe and 2 eV for BBCo, as shown in Table I. It is interesting to note that the binding strengths are stronger than on graphene [69], but weaker than that previously obtained on the β_{12} borophene monolayer [70]. At the equilibrium geometry, the M adatom is located at the center of the hollow hexagon, with M—B distance close to the sum of their covalent radii, suggesting covalent bonds. However, charge-density plots indicate an ionic interaction (see Fig. S1 within the Supplemental Material [71]).

Figure 2 shows the electronic band structure of pristine BB and the doped systems, BBFe and BBCo. We find that BB is a semiconductor with a direct band gap of 0.7 eV, according to our PBE+U calculations [Fig. 2(a)]. Additional calculations with the hybrid functional HSE06 were performed to validate these results, giving a direct

TABLE I. Binding energy (E_b), shortest average M—B bond distances (d_{M-B}), M height (Δz), and work function (Φ) of M adatom on bilayer borophene for metal coverages $\theta = 1/4$ (BBM$_{1/4}$) and $\theta = 1$(BBM$_1$); m is the magnetic moment per M atom.

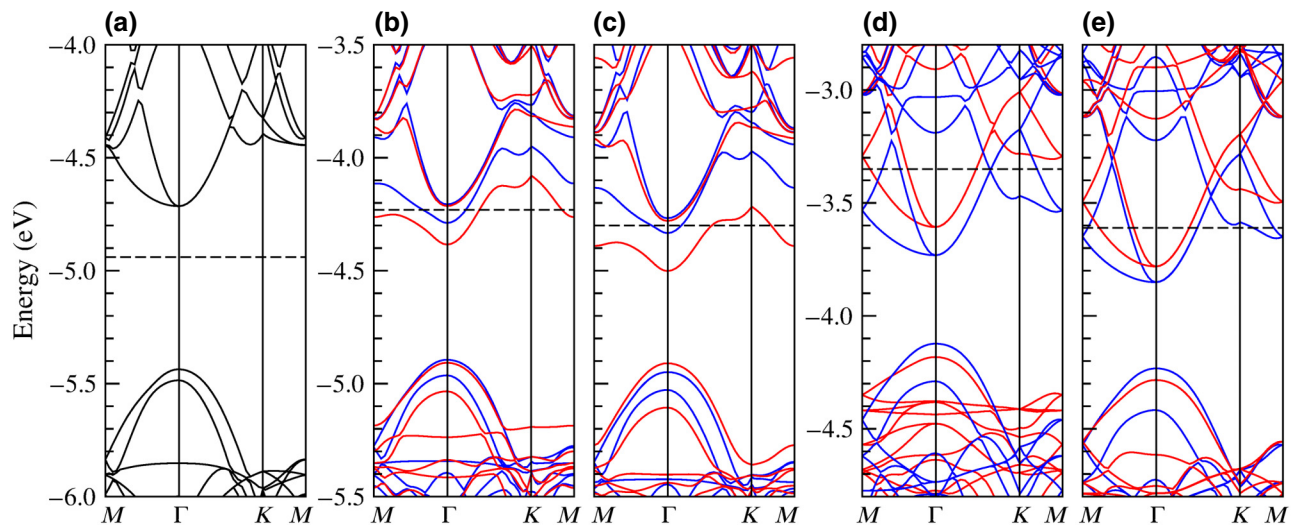| System	E_b (eV)	d_{M-B} (Å)	Δz (Å)	Φ (eV)	m (μ_B)
BBFe$_{1/4}$	−3.08	2.21	1.52	4.23	2.71
BBFe$_1$	−2.83	2.22	1.56	3.54	3.26
BBCo$_{1/4}$	−2.36	2.18	1.53	4.30	1.50
BBCo$_1$	−2.13	2.18	1.52	3.61	2.12

FIG. 2.   Electronic band structures of free-standing bilayer borophene (BB) with Fe and Co adatoms at the hollow hexagon site. (a) Pristine BB, (b) BBFe$_{1/4}$, (c) BBCo$_{1/4}$, (d) BBFe$_1$, and (e) BBCo$_1$. The zero energy is set at the vacuum level. Red and blue curves indicate spin-up and spin-down bands. The dashed line indicates the Fermi energy.

band gap of 1.1 eV (see Table S1 and Fig. S2 within the Supplemental Material [71]). Apart from the small difference of 0.4 eV in the BB band gap, similar band-structure characteristics are observed, not only for BB but also for BBM, suggesting that the PBE+U method can reasonably address the on-site $3d$ electron-electron interaction.

After the Fe and Co adsorption on BB, both BBFe and BBCo become metallic for the two metal coverages under study, as shown in Figs. 2(b) and 2(c). The metal atom induces a magnetization due to the unpaired M-$3d$ electrons, promoting the formation of spin-polarized metallic bands close to the Fermi level. We also observe that the magnetic moment of the system changes with the coverage; for BBFe$_{1/4}$ and BBFe$_1$, it increases from $m = 2.7$ to $3.3\mu_B$, indicating a spin coupling among Fe adatoms due to its proximity. The same is observed for the Co adatoms, where the magnetic moment of BBCo$_{1/4}$ and BBCo$_1$ increases from $m = 1.5$ to $2.1\mu_B$. It is worth noting that the host's B-$2p$ orbitals make the largest contribution to the metallic bands, with almost no contribution from the metal adatoms. The total density of states (DOS) and the DOS projected on the M-$3d$ orbitals confirm the above statement (see Fig. S3 within the Supplemental Material [71]).

We also calculate the work function (Φ), which is the energy needed to remove an electron from the Fermi level and put it in the vacuum. According to Fig. 2(a), a work function of pristine BB of 4.94 eV is found, in good agreement with experimental results [45]. However, for BBM$_{1/4}$ and BBM$_1$ we found Φ values of around 4.3 and 3.6 eV, respectively. We also note that the metal species has negligible effects on the work function, with a slight increase for BBCo concerning BBFe (see Table I). Therefore, BB with full metal coverage would show a decrease in the work

function by around 28%, while for the low metal coverage, it would be around 14%, indicating that the metal adatoms would enhance the electron transfer property of bilayer borophene.

B. O$_2$ and OOH interaction with the metal center of BBM

Next, we study the adsorption of O$_2$ and OOH molecules on the metal atom of BBM, hereafter referred to as O$_2^*$ and OOH*. Our results for both metal coverages are shown in Table II, where results on the Pt(111) surface are included for comparison. The first thing we notice is an increase in the binding strength of the molecules for higher metal concentrations, which is accompanied by a stretching of the O—O bond. For BBFe$_{1/4}$, O$_2$ attaches to Fe adatom in the side-on configuration with a binding energy of -1.63 eV. In contrast, the end-on configuration is unstable, evolving to the side-on one after relaxation. A magnetic moment of the Fe-O$_2$ adduct of $m = 4.1\mu_B$ is found. Considering that BBFe$_{1/4}$ and gas-phase O$_2$ have magnetic moments of $m = 2.7$ and $2.0\mu_B$, respectively, we infer that the Fe-O$_2$ adduct exhibits a high-spin coupling, that is O$_2$ would adopt a parallel spin configuration. For the BBFe$_1$, the binding energy of O$_2$ increases by around 0.34 eV, while the magnetization of the Fe-O$_2$ adduct decreases to $m = 2.9\mu_B$. Because the magnetization of BBFe$_1$ is $m = 3.3\mu_B$, we note that the Fe-O$_2$ adduct exhibits a low-spin coupling, that is O$_2$ would adopt an antiparallel spin configuration. Therefore, higher metal coverage on bilayer borophene tends to increase the O$_2$ binding strength, changing the spin coupling of the Fe-O$_2$ adduct. Concerning the OOH molecule, the binding strength also increases with the metal coverage, by 0.23 eV, but the spin coupling of the Fe-OOH adduct remains

TABLE II. Binding energy (E_b), dissociation energy (E_a), and bond distances (d) of O_2 and OOH molecules adsorbed on the M adatom on bilayer borophene for metal coverages $\theta = 1/4$ (BBM$_{1/4}$) and $\theta = 1$ (BBM$_1$); m is the magnetic moment per M atom. Results on Pt(111) surface are included for comparison.

System	E_b (eV)	E_a (eV)	$d_{O—O}$ (Å)	$d_{M—O}$ (Å)	m (μ_B)
(BBFe$_{1/4}$)–O$_2$	−1.63	0.98	1.38	1.97	4.10
(BBFe$_1$)–O$_2$	−1.97	1.33	1.44	1.87	2.91
(BBFe$_{1/4}$)–OOH	−2.38	0.57	1.49	1.86	3.28
(BBFe$_1$)–OOH	−2.61	0.47	1.50	1.89	3.29
(BBCo$_{1/4}$)–O$_2$	−1.41	1.36	1.38	1.87	1.56
(BBCo$_1$)–O$_2$	−1.72	1.30	1.41	1.87	1.71
(BBCo$_{1/4}$)–OOH	−2.08	0.53	1.49	1.84	2.01
(BBCo$_1$)–OOH	−2.21	0.81	1.52	1.84	2.02
Pt(111)–O$_2$	−0.51	0.60	1.37	2.08	0.00
Pt(111)–OOH	−1.10	0.03	1.46	2.03	0.00

unchanged. The same trend is observed for the O_2 and OOH adsorption on the Co adatom. Details of the results can be found in Table II.

The most probable reaction pathway for ORR initiates with the O_2 adsorption on the active site followed by the capture of a proton forming OOH*. Therefore, the OOH* stabilization and further dissociation are relevant to elucidate ORR activity on BBM. Thus, we calculate the dissociation energy of O_2^* and OOH* using the NEB method [57, 58], considering six intermediate images, where transition states were verified by vibrational frequency calculations.

Figure 3 shows the minimum energy path for the OOH dissociation on BBFe$_{1/4}$, BBCo$_{1/4}$, and on the Pt(111) surface. Our findings reveal dissociation energies of around 0.5 eV, whereas on Pt(111) the dissociation proceeds almost barrierless. These results contrast with those obtained for O_2^*, where dissociation energies are much larger, as shown in Table II and Fig. S4 within the Supplemental Material [71]. It is worth noting that the metal coverage of BBM also induces changes in O_2^* and OOH* adsorption strength and dissociation energies.

Several works have reported experimental evidence of a correlation between the nanoscale work function and the catalytic activity in doped and defective nanocarbon electrocatalysts [28–30]. However, according to other results, the influence of the work function varies from one system to another [72,73]. In our study, we found that work function decreases with the Fe and Co concentration on BB by around 0.7 eV (see Table I). However, the O_2^* and OOH* dissociation energies, which we associated with the ORR activity, tend to increase for BBFe$_1$ and decrease for BBCo$_1$ (see Table II). Therefore, we cannot establish a correlation between BBM work function and adsorbate dissociation energies.

C. Oxygen-reduction reaction activity on BB and BBM

According to our results, the O_2^* dissociation energy is found to be relatively high as compared with OOH*,

almost doubling its value, suggesting that ORR would not evolve from the direct O_2^* dissociation, requiring the capture of a proton. Therefore, a probable pathway that has been considered for the O_2 reduction on BBM would involve the OOH*, O*, and OH* intermediates, according to the reactions:

$$O_2 + BBM \rightleftharpoons O_2^* \qquad (1)$$

$$O_2^* + H^+ + e^- \rightleftharpoons OOH^* \qquad (2)$$

$$OOH^* + H^+ + e^- \rightleftharpoons O^* + H_2O \qquad (3)$$

$$O^* + H^+ + e^- \rightleftharpoons OH^* \qquad (4)$$

$$OH^* + H^+ + e^- \rightleftharpoons BBM + H_2O \qquad (5)$$

The ORR performance on the metal center of BBM was assessed through the adsorption free energy of the reaction intermediates OOH*, O*, and OH* within the CHE model [59]. We have included in this analysis the pristine BB surface to elucidate its possible ORR activity. From the thermodynamics point of view, all elementary reduction reaction steps proceed spontaneously at zero potential relative to the reversible hydrogen electrode ($U = 0$ V). At the equilibrium potential ($U = 1.23$ V) the free energy is downshifted by the number of (H$^+$, e^-) pairs involved in each elementary step. The potential at which all the reaction steps are downhill in free energy is defined as the onset potential (U_{onset}). The theoretical overpotential (η_{theo}) can be obtained from the difference between the equilibrium potential and the U_{onset}, which is a measure of the ORR electrocatalytic performance [74]. Calculation details are given within the Supplemental Material [71], here Table S2 summarizes adsorption free energies of the ORR intermediates and the η_{theo} calculations for pristine BB and BBM for both coverages, which were performed with the hybrid HSE functional. In these calculations, we include correction by solvation effects, which involve the addition of 0.3 eV to the adsorption free energy of OH* and OOH*, weakening their strength. This correction takes care
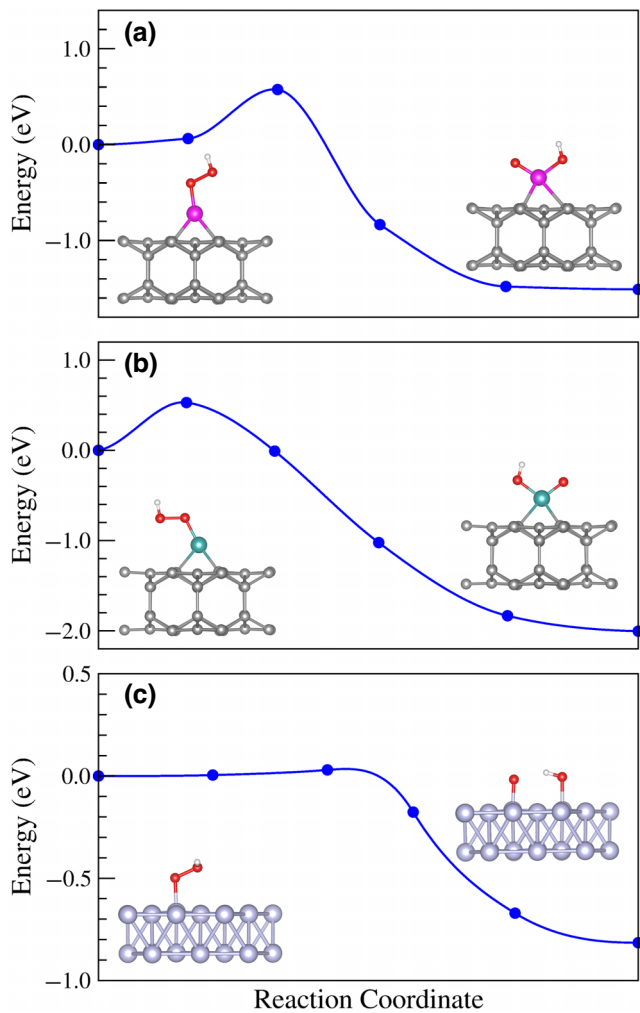
FIG. 3. Minimum energy path for the OOH* dissociation on (a) the Fe adatom of BBFe$_{1/4}$, (b) the Co adatom of BBCo$_{1/4}$, and (c) the Pt(111) surface. Inset figures display the initial and final equilibrium geometries.
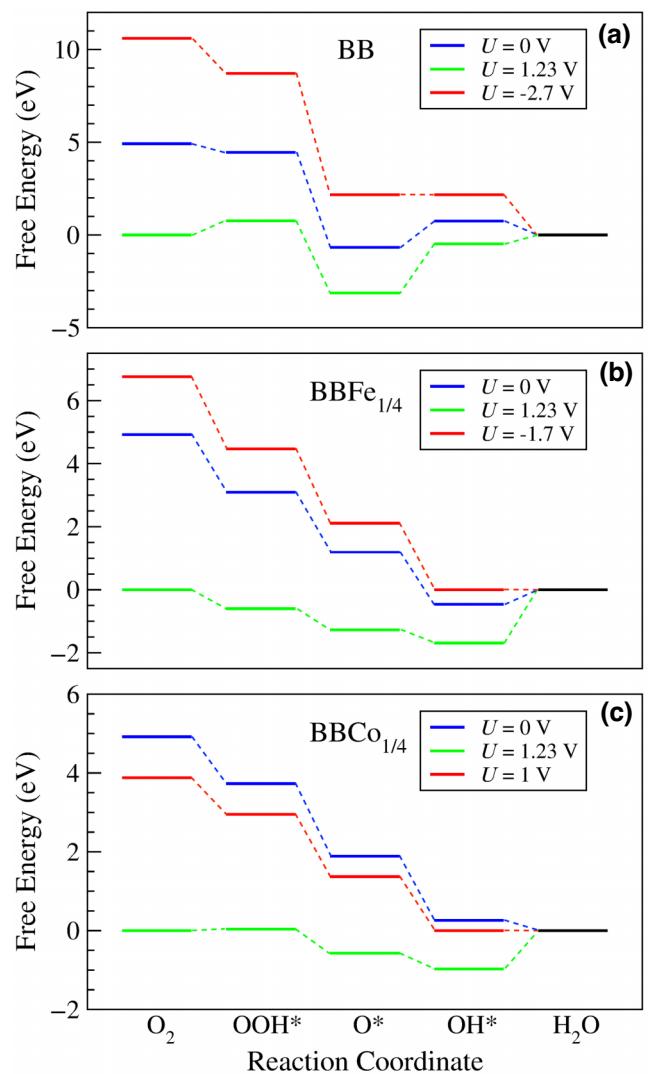

FIG. 4. Reaction free energy diagrams for the ORR intermediates at different electrode potential versus reversible hydrogen electrode for (a) pristine BB, (b) BBFe$_{1/4}$, and (c) BBCo$_{1/4}$. The red lines represent the onset potential at which all reaction steps are downhill in free energy.

of the solvent interaction, according to previous studies on similar single-atom catalysts [75–77].

Figure 4 shows the reaction free-energy diagrams of the ORR on pristine BB, BBFe$_{1/4}$, and BBCo$_{1/4}$ for different electrode potentials. The red lines represent the onset potential at which all reaction steps are downhill in free energy. Results for BBFe$_1$ and BBCo$_1$ are shown in Fig. S5 within the Supplemental Material [71]. Our findings reveal rate-determining steps at O* → OH* for BB and at OH* → H$_2$O for BBFe and BBCo. The theoretical onset potential on BB, BBFe$_{1/4}$, and BBFe$_1$ are quite large, indicating no or limited ORR activity. However, on BBCo$_{1/4}$ and BBCo$_1$ they are found of 0.26 and 0.03 V, with theoretical overpotentials of $\eta_{\text{theo}} = 0.97$ and 1.20 V, respectively. These results are close to those reported for Pt(111) of 0.4 V [74], and for the FeN$_4$ center in graphene of 0.42 V [77], using the same methodology. Based on our

findings, only BBCo would show competitive ORR activity. This is contingent upon the metal coverage, which can be linked to variations in the adsorption strength of the OH* intermediate, suggesting a mechanism to improve the overpotential.

The above results were obtained with the hybrid HSE06 functional, which is known to be more accurate for a broader range of materials, including those with strongly correlated electrons like 3d transition metals. We also consider the PBE+U approach to test its accuracy. In Fig. S6 within the Supplemental Material [71], the reaction free-energy diagrams for ORR intermediates on BBM calculated with both HSE06 and PBE+U functionals, considering the same solvent correction, are given. We observe that

the HSE06 functional tends to describe the ORR interme-
diates more strongly bound to the metal than the PBE+U
functional, with energy differences reaching around 0.8 eV
for O*. The case of OH* is the exception, exhibiting sim-
ilar adsorption free energy for both functionals, especially
for BBFe.

D. Stability of BB and BBM in solution through Pourbaix analysis

To gain insight into the electrochemical stability of pris-
tine BB and BBM systems in acidic and alkaline environ-
ments, we constructed Pourbaix diagrams for the electrode
potential considering O, OH, and H adsorbates as a func-
tion of the pH, according to the Nerst equation. Details of
calculations are presented within the Supplemental Mate-
rial [71]. The standard potentials for BBM dissolution and
BB corrosion, which are independent of pH, were obtained
from the calculated electronic work functions, using the
linear correlation between work functions and the stan-
dard reduction potential, recently reported by Li *et al.* [78].
In the Pourbaix diagrams, the stable phases were identi-
fied following the rule that the most stable oxidized phase
had the lowest equilibrium potential, while the most stable
reduced phase had the highest equilibrium potential [66].

Figure 5 shows the Pourbaix diagrams for pristine BB,
BBFe$_{1/4}$, and BBCo$_{1/4}$. For BB our results reveal oxi-
dation at any pH, where O* would be the species ener-
getically favorable, covering the surface while preserv-
ing its integrity. For and BBFe$_{1/4}$, OH* would saturate
the Fe adatom, preserving the BBFe integrity. Whereas,
BBCo$_{1/4}$ would suffer demetallation in acidic media, while
for pH > 8, it would be stable. Therefore, the ORR activ-
ity of BBCo$_{1/4}$ would be only possible in alkaline media.
Pourbaix diagrams for the full metal coverage BBFe$_1$ and
BBCo$_1$ are given in Fig. S7 within the Supplemental Mate-
rial [71]. Our results reveal that BBFe$_1$ would preserve
its integrity for pH > 2, being saturated by OH* species,
while BBCo$_1$ would be demetallized for a wide pH range
(pH < 12). Therefore, according to surface Pourbaix dia-
grams, BBCo$_{1/4}$ would exhibit ORR activity but only in
alkaline media, while the BB surface surrounding the Co
adatom would be oxidized by O and OH species.

E. Stability of BB and BBM in solution through AIMD simulations

To study the stability of BBFe and BBFe-O$_2$ systems
in solution at operational conditions, we added explicit
water molecules to our system at the experimental den-
sity (1 g/cm^3) and performed AIMD simulations at 300
K. The characterization of liquid water was examined
within a box containing 100 H$_2$O molecules by plotting the
radial distribution function and comparing it with avail-
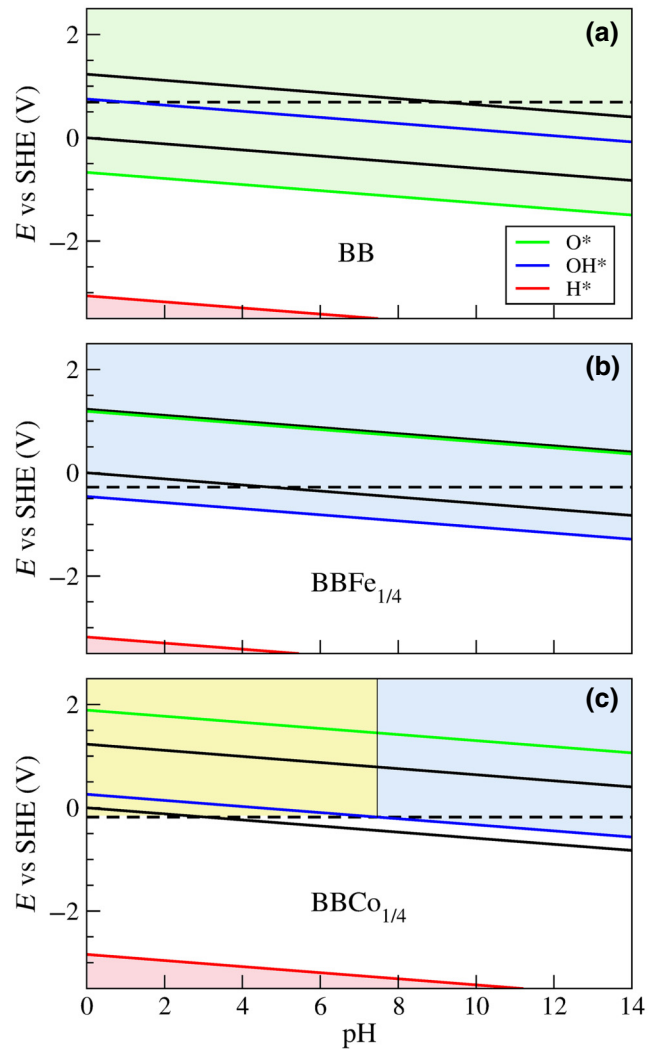able experimental data [79,80]. Our findings suggest a

FIG. 5. Surface Pourbaix diagram of the electrode potential
versus the standard hydrogen electrode (SHE) as a function of
pH for (a) pristine BB, (b) BBFe$_{1/4}$, and (c) BBCo$_{1/4}$. The
area between the black lines represents the water-stability region
(upper H$_2$O/O$_2$, lower H$^+$/H$_2$). The dashed line indicates the
dissolution potential and the yellow area is the unstable region of
metal dissolution.

satisfactory description, detailed within the Supplemental
Material [71].

We consider two initial geometries for the AIMD sim-
ulation: (i) with the O$_2$ molecule far from the Fe cen-
ter surrounded by water molecules, and (ii) with the O$_2$
molecule attached to the Fe center (O$_2^*$). Our results indi-
cate that in both cases the BBFe structure maintains its
integrity throughout the simulation. In case (i), a snapshot
taken at 6 ps indicates that three H$_2$O weakly attach to
the Fe center while O$_2$ remains far away surrounded by
water molecules. In case (ii), O$_2^*$ captures a proton form-
ing OOH*, and subsequently a H$_2$O weakly joints to the
OOH*. This configuration is maintained during the rest of

the simulation time. The snapshot at 6 ps and the free-energy evolution are shown in Figs. S8 and S9 within the Supplemental Material [71].

Our simulation of BBFe-O_2 in water can be interpreted as being in alkaline media, given the absence of protons. However, improved ORR activity is anticipated in acidic media. In acidic conditions, there is a higher probability that O_2^* captures a proton, transforming into OOH^*. This expectation is grounded in the fact that OOH^* exhibits significantly lower dissociation energy compared to O_2^*, as demonstrated by our static results. To verify this, we simulate a specific acidic medium, adding hydrochloric acid into water (an HCl molecule), resulting in a concentration of around 1 M, as shown Fig. 6(a). As this AIMD simulation starts, HCl dissociates rapidly, where Cl^- becomes surrounded by water molecules and H^+ jumps from H_2O to H_2O, forming hydronium (H_3O^+). The free-energy evolution is shown in Fig. 6(c), where numbers in parentheses indicate key reaction steps. Once H^+ approaches O_2^*, an OOH^* is formed, which rapidly dissociates expelling an OH^- radical [step (1)], somehow corroborating the

proposed mechanism for ORR in our simplified model. As the AIMD simulation continues, O^* captures two protons consecutively, becoming OH^* and then H_2O^* [step (2)]. Finally, a second H_2O molecule approaches the Fe atom, forming the $2(H_2O)^*$ adsorbate [step (5)]. In the meantime, an O atom and an OH radical attach to the BB surface [steps (3) and (4)], respectively. This configuration is achieved within the first 2.5 ps and is maintained during the rest of the simulation time. A snapshot at 6 ps shows the geometry, which is displayed in Fig. 6(b). Hence, our AIMD simulation suggests that BBM systems would exhibit stability in solution under standard conditions for this specific acidic medium, thereby demonstrating ORR activity.

Furthermore, we assess the stability of pristine BB in explicit acidic and alkaline environments through AIMD simulation. In the alkaline medium, we examine its behavior in pure water, whereas, for the acidic medium, we investigate its response in a hydrochloric solution at approximately 3 M by including 4 HCl molecules in our system. In both environments, the surface of BB remains undamaged after 6 ps of simulation time, as illustrated in Figs. S10 and S11 within the Supplemental Material [71]. Nevertheless, we observe the presence of O^* and OH^* species on the BB surface, indicating an ongoing oxidation process. This observation aligns with the BB-O and BB-OH potential in the Pourbaix diagram of pristine BB, as depicted in Fig. 5(a).
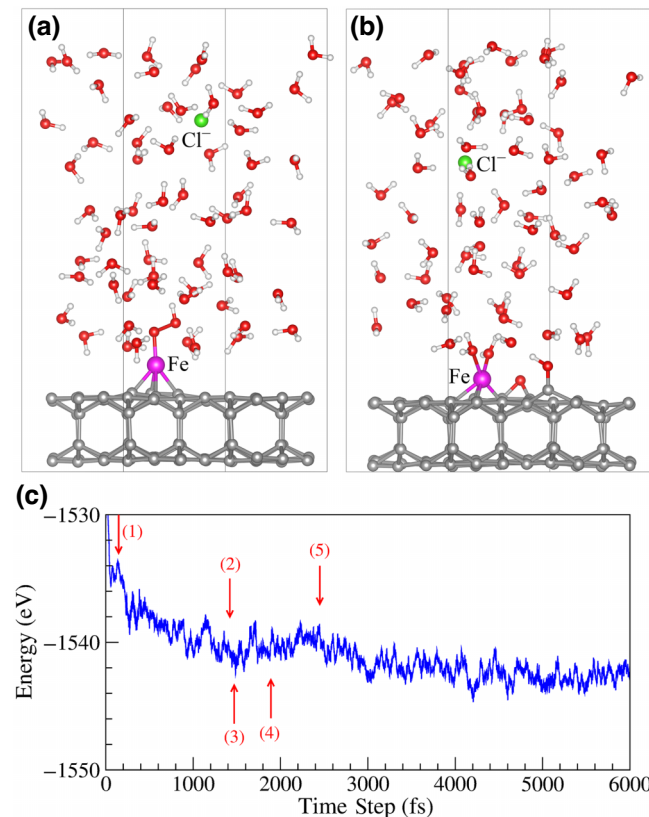
F. BB and BBM interaction with the Ag(111) substrate

Finally, we investigate the interaction of the substrate supporting the BBM structures and its effect on the adsorbates. We consider the Ag(111) substrate, which is where BB was grown experimentally [45]. Ag(111) was simulated with a (4×4) surface unit cell with four monolayers, using the same methodology as Pt(111) described above. We found a mismatch between Ag(111) and BB of 4.5%, which was resolved by compressing the BB structure. We found that BB is weakly attached to the Ag(111) surface by van der Waals interaction, as shown in Figs. S13 and S14 within the Supplemental Material [71], with a binding energy of -43 meV/$Å^2$, in close agreement with previous results [45,81]. This finding strongly supports the possibility of successfully exfoliating BB from the Ag(111) surface [82].

Furthermore, we introduced Fe and Co atoms into the hollow site of BB, following the $BBM_{1/4}$ coverage pattern. Interestingly, we observed a slight decrease in the binding energy of $BBM_{1/4}$ on Ag(111) compared to pristine BB, approximately by 2 meV/$Å^2$. Then, we investigated the adsorption of O_2 on the M adatoms of Ag(111)-supported $BBM_{1/4}$. Here, we found a binding energy roughly 0.1 eV lower than that observed on free-standing $BBM_{1/4}$. Consequently, we can conclude that the presence of the Ag(111)

FIG. 6. AIMD simulation at 300 K of BBFe-O_2 in hydrochloric acid solution. (a) Initial geometry with Cl^- surrounded by water plus the OOH^* adsorbate. (b) Snapshot at 6 ps of simulation time. (c) Energy evolution during 6 ps of simulation time. The numbers in parentheses indicate key reaction steps described in the text.

substrate has minimal effect on the binding strength of adsorbates on $BBFe_{1/4}$ and $BBCo_{1/4}$, suggesting that the catalytic activity for the ORR would be unaffected by the BBM substrate.

IV. SUMMARY AND CONCLUSIONS

In summary, we have studied the stability, electronic properties, and ORR catalytic activity of Fe and Co adatoms on free-standing bilayer borophene, using DFT calculations and AIMD simulations. The electronic band structures indicate that BB is a two-dimensional semiconductor with a direct band gap of 1.1 eV. However, after the metal incorporation, it becomes metallic, facilitating charge transport. The metal adatoms reduce the work function of pristine BB by around 14% for the low metal coverage ($BBM_{1/4}$), and by 28% for the full metal coverage (BBM_1), thereby enhancing the electron transfer with the metal coverage. Regarding the strength of adsorbate species, the low dissociation energy observed for OOH* as compared with O_2^* suggests that the ORR activity would likely proceed after a proton capture by O_2^*. The energetics of key ORR intermediates suggest that only low-coverage metal adatom would exhibit competitive ORR activity, particularly $BBCo_{1/4}$, which shows the best results with a theoretical overpotential of around 1 V. However, this activity would be only possible in alkaline environments where the $BBCo_{1/4}$ structure remains stable. Additionally, the high-coverage structure $BBCo_1$ also exhibits ORR activity but it would be unstable in a wide range of pH. We attribute this behavior to the lower work function exhibited by the full-coverage BBM structures, promoting easy charge transfer and demetallation. Molecular dynamics simulations confirm the stability and ORR activity for specific acidic and alkaline environments. Ultimately, the results obtained using the PBE+U functional were compared with those obtained through the HSE functional whenever possible. Our findings suggest that DFT+U yields reasonably accurate results in specific systems; however, it does not represent a general trend and is contingent upon the particular system under study.

ACKNOWLEDGMENTS

---

[1] B. C. H. Steele and A. Heinzel, Materials for fuel-cell technologies, Nature **414**, 345 (2001).

[2] M. C. Debe, Electrocatalyst approaches and challenges for automotive fuel cells, Nature **486**, 43 (2012).

[3] Y. Chen, S. Ji, S. Zhao, W. Chen, J. Dong, W.-C. Cheong, R. Shen, X. Wen, L. Zheng, and A. I. Rykov, *et al.*, Enhanced oxygen reduction with single-atomic-site iron catalysts for a zinc-air battery and hydrogen-air fuel cell, Nat. Commun. **9**, 5422 (2018).

[4] J. Wu and H. Yang, Platinum-based oxygen reduction electrocatalysts, Acc. Chem. Res. **46**, 1848 (2013).

[5] S. Hussain, H. Erikson, N. Kongi, A. Sarapuu, J. Solla-Gullón, G. Maia, A. M. Kannan, N. Alonso-Vante, and K. Tammeveski, Oxygen reduction reaction on nanostructured Pt-based electrocatalysts: A review, Int. J. Hydrog. Energy **45**, 31775 (2020).

[6] R. Bashyam and P. Zelenay, A class of non-precious metal composite catalysts for fuel cells, Nature **443**, 63 (2006).

[7] G. Wu, K. L. More, C. M. Johnston, and P. Zelenay, High-performance electrocatalysts for oxygen reduction derived from polyaniline, iron, and cobalt, Science **332**, 443 (2011).

[8] C.-X. Zhao, B.-Q. Li, J.-N. Liu, and Q. Zhang, Intrinsic electrocatalytic activity regulation of *M*-N-C single-atom catalysts for the oxygen reduction reaction, Angew. Chem. Int. Ed. **60**, 4448 (2021).

[9] R. Jasinski, A new fuel cell cathode catalyst, Nature **201**, 1212 (1964).

[10] G. Abarca, W. Orellana, M. Viera, C. Aliaga, J. F. Marco, J. H. Zagal, and F. Tasca, In search of the most active MN4 catalyst for the oxygen reduction reaction. The case of perfluorinated Fe phthalocyanine, J. Mater. Chem. A **7**, 24776 (2019).

[11] C. Z. Loyola, G. Abarca, S. Ureta-Zañartu, C. Aliaga, J. H. Zagal, M. T. Sougrati, F. Jaouen, W. Orellana, and F. Tasca, Insights into the electronic structure of Fe penta-coordinated complexes. Spectroscopic examination and electrochemical analysis for the oxygen reduction and oxygen evolution reactions, J. Mater. Chem. A **9**, 23802 (2021).

[12] W. Orellana, C. Z. Loyola, J. F. Marco, and F. Tasca, Evidence of carbon-supported porphyrins pyrolyzed for the oxygen reduction reaction keeping integrity, Sci. Rep. **12**, 8072 (2022).

[13] M. Lefèvre, E. Proietti, F. Jaouen, and J.-P. Dodelet, Iron-based catalysts with improved oxygen reduction activity in polymer electrolyte fuel cells, Science **324**, 71 (2009).

[14] F. Calle-Vallejo, J. I. Martínez, and J. Rossmeisl, Density functional studies of functionalized graphitic materials with late transition metals for oxygen reduction reactions, Phys. Chem. Chem. Phys. **13**, 15639 (2011).

[15] D. H. Lee, W. J. Lee, W. J. Lee, S. O. Kim, and Y.-H. Kim, Theory, synthesis, and oxygen reduction catalysis of Fe-porphyrin-like carbon nanotube, Phys. Rev. Lett. **106**, 175502 (2011).

[16] H. R. Byon, J. Suntivich, and Y. Shao-Horn, Graphene-based non-noble-metal catalysts for oxygen reduction reaction in acid, Chem. Mater. **23**, 3421 (2011).

[17] Y. Li, W. Zhou, H. Wang, L. Xie, Y. Liang, F. Wei, J.-C. Idrobo, S. J. Pennycook, and H. Dai, An oxygen reduction electrocatalyst based on carbon nanotube-graphene complexes, Nat. Nanotech. **7**, 394 (2012).

[18] W. Orellana, Catalytic properties of transition metal-N_4 moieties in graphene for the oxygen reduction reaction:

Evidence of spin-dependent mechanisms, J. Phys. Chem. C **117**, 9812 (2013).

[19] S. Kattel and G. Wang, Reaction pathway for oxygen reduction on FeN_4 embedded graphene, J. Phys. Chem. Lett. **5**, 452 (2014).

[20] L. Wu, X. Cao, W. Hu, Y. Ji, Z.-Z. Zhu, and X.-F. Li, Improving the oxygen reduction reaction activity of FeN_4-graphene via tuning electronic characteristics, ACS Appl. Energy Mater. **2**, 6634 (2019).

[21] H.-Y. Zhuo, X. Zhang, J.-X. Liang, Q. Yu, H. Xiao, and J. Li, Theoretical understandings of Graphene-based metal single-atom catalysts: Stability and catalytic performance, Chem. Rev. **120**, 12315 (2020).

[22] W. Ju, A. Bagger, G. P. Hao, A. S. Varela, I. Sinev, V. Bon, B. R. Cuenya, S. Kaskel, J. Rossmeisl, and P. Strasser, Understanding activity and selectivity of metal-nitrogen-doped carbon catalysts for electrochemical reduction of CO_2, Nat. Commun. **8**, 944 (2017).

[23] A. S. Varela, W. Ju, A. Bagger, P. Franco, J. Rossmeisl, and P. Strasser, Electrochemical reduction of CO_2 on metal-nitrogen-doped carbon catalysts, ACS Catal. **9**, 7270 (2019).

[24] Y. Xu, A. V. Ruban, and M. Mavrikakis, Adsorption and dissociation of O_2 on Pt-Co and Pt-Fe alloys, J. Am. Chem. Soc. **126**, 4717 (2004).

[25] L. Qi, X. Qian, and J. Li, Near neutrality of an oxygen molecule adsorbed on a Pt(111) surface, Phys. Rev. Lett. **101**, 146101 (2008).

[26] Z. Duan and G. Wang, A first principles study of oxygen reduction reaction on a Pt(111) surface modified by a subsurface transition metal M ($M = Ni, Co,$ or Fe), Phys. Chem. Chem. Phys. **13**, 20178 (2011).

[27] C. G. Vayenas, S. Bebelis, and S. Ladas, Dependence of catalytic rates on catalyst work function, Nature **343**, 625 (1990).

[28] J. Y. Cheon, J. H. Kim, J. H. Kim, K. C. Goddeti, J. Y. Park, and S. H. Joo, Intrinsic relationship between enhanced oxygen reduction reaction activity and nanoscale work function of doped carbons, J. Am. Chem. Soc. **136**, 8875 (2014).

[29] Y. Cai, L. Tao, G. Huang, N. Zhang, Y. Zou, and S. Wang, Regulating carbon work function to boost electrocatalytic activity for the oxygen reduction reaction, Chinese J. Cat. **42**, 938 (2021).

[30] H. Radinger, V. Trouillet, F. Bauer, and F. Scheiba, Work function describes the electrocatalytic activity of graphite for vanadium oxidation, ACS Catal. **12**, 6007 (2022).

[31] A. J. Mannix, X.-F. Zhou, B. Kiraly, J. D. Wood, D. Alducin, B. D. Myers, X. Liu, B. L. Fisher, U. Santiago, and J. R. Guest, *et al.*, Synthesis of borophenes: Anisotropic, two-dimensional boron polymorphs, Science **350**, 1513 (2015).

[32] B. Feng, J. Zhang, Q. Zhong, W. Li, S. Li, H. Li, P. Cheng, S. Meng, L. Chen, and K. Wu, Experimental realization of two-dimensional boron sheets, Nat. Chem. **8**, 563 (2016).

[33] B. Kiraly, X. Liu, L. Wang, Z. Zhang, A. J. Mannix, B. L. Fisher, B. I. Yakobson, M. C. Hersam, and N. P. Guisinger, Borophene synthesis on Au(111), ACS Nano **13**, 3816 (2019).

[34] H. Tang and S. Ismail-Beigi, First-principles study of boron sheets and nanotubes, Phys. Rev. B **82**, 115412 (2010).

[35] X. Wu, J. Dai, Y. Zhao, Z. Zhuo, J. Yang, and X. C. Zeng, Two-dimensional boron monolayer sheets, ACS Nano **6**, 7443 (2012).

[36] F. Ma, Y. Jiao, G. Gao, Y. Gu, A. Bilic, Z. Chen, and A. Du, Graphene-like two-dimensional ionic boron with double dirac cones at ambient condition, Nano Lett. **16**, 3022 (2016).

[37] X.-F. Zhou, A. R. Oganov, Z. Wang, I. A. Popov, A. I. Boldyrev, and H.-T. Wang, Two-dimensional magnetic boron, Phys. Rev. B **93**, 085406 (2016).

[38] H. Zhong, K. Huang, G. Yu, and S. Yuan, Electronic and mechanical properties of few-layer borophene, Phys. Rev. B **98**, 054104 (2018).

[39] N. Gao, X. Wu, X. Jiang, Y. Bai, and J. Zhao, Structure and stability of bilayer borophene: The roles of hexagonal holes and interlayer bonding, FlatChem **7**, 48 (2018).

[40] S.-G. Xu, B. Zheng, H. Xu, and X.-B. Yang, Ideal nodal line semimetal in a two-dimensional boron bilayer, J. Phys. Chem. C **123**, 4977 (2019).

[41] S. M. Mozvashi, M. R. Givi, and M. B. Tagani, The effects of substrate and stacking in bilayer borophene, Sci. Rep. **12**, 13661 (2022).

[42] Y. Xu, X. Xuan, T. Yang, Z. Zhang, S.-D. Li, and W. Guo, Quasi-freestanding bilayer borophene on Ag(111), Nano Lett. **22**, 3488 (2022).

[43] R. Yang and M. Sun, Bilayer borophene synthesized on Ag(111) film: Physical mechanism and applications for optical sensor and thermoelectric devices, Mater. Today Phys. **23**, 100652 (2022).

[44] N. Gao, J. Li, J. Chen, and X. Yang, Interaction between bilayer borophene and metal or inert substrates, Appl. Surf. Sci. **626**, 157157 (2023).

[45] X. Liu, Q. Li, Q. Ruan, M. S. Rahn, B. I. Yakobson, and M. C. Hersam, Borophene synthesis beyond the single-atomic-layer limit, Nat. Mater. **21**, 35 (2022).

[46] C. Chen, H. Lv, P. Zhang, Z. Zhuo, Y. Wang, C. Ma, W. Li, X. Wang, B. Feng, and P. Cheng, *et al.*, Synthesis of bilayer borophene, Nat. Chem. **14**, 25 (2022).

[47] Y.-Y. Ma, X.-Y. Zhao, W. Zan, Y. Mu, Z. Zhang, and S.-D. Li, Prediction of freestanding semiconducting bilayer borophenes, Nano Res. **15**, 5752 (2022).

[48] H.-R. Zhu, Y.-L. Hu, S.-H. Wei, and D.-Y. Hua, Single-metal atom anchored on boron monolayer (β_{12}) as an electrocatalyst for nitrogen reduction into ammonia at ambient conditions: A first-principles study, J. Phys. Chem. C **123**, 4274 (2019).

[49] C. Liu, Q. Li, J. Zhang, Y. Jin, D. R. MacFarlane, and C. Sun, Conversion of dinitrogen to ammonia on Ru atoms supported on boron sheets: A DFT study, J. Mater. Chem. A **7**, 4771 (2019).

[50] P. Zhang, X. Xu, E. Song, X. Hou, X. Yang, J. Mi, J. Huang, and C. Stampfl, Transition metal-doped α-borophene as potential oxygen and hydrogen evolution electrocatalyst: A density functional theory study, Catal. Commun. **144**, 106090 (2020).

[51] P. Giannozzi, S. Baroni, N. Bonini, M. Calandra, R. Car, C. Cavazzoni, D. Ceresoli, G. L. Chiarotti, M. Cococcioni, and I. Dabo, *et al.*, QUANTUM ESPRESSO: A modular and open-source software project for quantum simulations of materials, J. Phys.: Condens. Matter **21**, 395502 (2009).

[52] P. Giannozzi, O. Andreussi, T. Brumme, O. Bunau, M. Buongiorno Nardelli, M. Calandra, R. Car, C. Cavazzoni, D. Ceresoli, and M. Cococcioni, *et al.*, Advanced capabilities for materials modelling with quantum espresso, J. Phys.: Condens. Matter **29**, 465901 (2017).

[53] J. P. Perdew, K. Burke, and M. Ernzerhof, Generalized gradient approximation made simple, Phys. Rev. Lett. **77**, 3865 (1996).

[54] M. Dion, H. Rydberg, E. Schröder, D. C. Langreth, and B. I. Lundqvist, van der Waals density functional for general geometries, Phys. Rev. Lett. **92**, 246401 (2004).

[55] H. J. Kulik, Perspective: Treating electron overdelocalization with the DFT+U method, J. Chem. Phys. **142**, 240901 (2015).

[56] M. J. van Setten, M. Giantomassi, E. Bousquet, M. J. Verstraete, D. R. Hamann, X. Gonze, and G.-M. Rignanese, The PseudoDojo: Training and grading a 85 element optimized norm-conserving pseudopotential table, Comput. Mater. Sci. **226**, 39 (2018).

[57] G. Henkelman, B. P. Uberuaga, and H. Jónsson, A climbing image nudged elastic band method for finding saddle points and minimum energy paths, J. Chem. Phys. **113**, 9901 (2000).

[58] G. Henkelman and H. A. Jónsson, Improved tangent estimate in the nudged elastic band method for finding minimum energy paths and saddle points, J. Chem. Phys. **113**, 9978 (2000).

[59] J. K. Nørskov, J. Rossmeisl, A. Logadottir, L. Lindqvist, J. R. Kitchin, T. Bligaard, and H. Jónsson, Origin of the overpotential for oxygen reduction at a fuel-cell cathode, J. Phys. Chem. B **108**, 17886 (2004).

[60] P. E. Blöchl, Projector augmented-wave method, Phys. Rev. B **50**, 17953 (1994).

[61] J. Heyd, G. E. Scuseria, and M. Ernzerhof, Hybrid functionals based on a screened coulomb potential, J. Chem. Phys. **118**, 8207 (2003).

[62] J. Heyd, G. E. Scuseria, and M. Ernzerhof, Erratum: Hybrid functionals based on a screened coulomb potential [J. Chem. Phys. 118, 8207 (2003)], J. Chem. Phys. **124**, 219906 (2006).

[63] A. Minguzzi, F.-R. F. Fan, A. Vertova, S. Rondinini, and A. J. Bard, Dynamic potential-pH diagrams application to electrocatalysts for water oxidation, Chem. Sci. **3**, 217 (2012).

[64] Z. Zeng, M. K. Y. Chan, Z.-J. Zhao, J. Kubal, D. Fan, and J. Greeley, Towards first principles-based prediction of highly accurate electrochemical Pourbaix diagrams, J. Phys. Chem. C **119**, 18177 (2015).

[65] G. Jerkiewicz, Standard and reversible hydrogen electrodes: Theory, design, operation, and applications, ACS Catal. **10**, 8409 (2020).

[66] A. S. Dobrota, N. V. Skorodumova, S. V. Mentus, and I. A. Pasti, Surface Pourbaix plots of M@N4-graphene single-atom electrocatalysts from density functional theory thermodynamic modeling, Electrochim. Acta **412**, 140155 (2022).

[67] S. Grimme, J. Antony, S. Ehrlich, and S. Krieg, A consistent and accurate ab initio parametrization of density functional dispersion correction (DFT-D) for the 94 elements H-Pu, J. Chem. Phys. **132**, 154104 (2010).

[68] S. Grimme, S. Ehrlich, and L. Goerigk, Effect of the damping function in dispersion corrected density functional theory, Comput. Chem. **32**, 1456 (2011).

[69] Y. Mao, J. Yuan, and J. Zhong, Density functional calculation of transition metal adatom adsorption on graphene, J. Phys. Condens. Matter **20**, 115209 (2008).

[70] J. C. Alvarez-Quiceno, G. R. Schleder, E. Marinho, and A. Fazzio, Adsorption of 3d, 4d, and 5d transition metal atoms on β_{12}-borophene, J. Phys. Condens. Matter **29**, 305302 (2017).

[71] See Supplemental Material at http://link.aps.org/supplemental/10.1103/PhysRevApplied.21.034008 for checks of convergence regarding structural and electronic properties using both the GGA+U and HSE functionals. Additionally, you will find detailed calculation procedures for ORR activity and Pourbaix analysis.

[72] A. M. Ismail, E. Csapó, and C. Janáky, Correlation between the work function of Au–Ag nanoalloys and their electrocatalytic activity in carbon dioxide reduction, Electrochim. Acta **313**, 171 (2019).

[73] T. Liu, C. Xi, C. Dong, C. Cheng, J. Qin, S. Hu, H. Liu, and X.-W. Du, Improving interfacial electron transfer via tuning work function of electrodes for electrocatalysis: From theory to experiment, J. Phys. Chem. C **123**, 28319 (2019).

[74] A. Kulkarni, S. Siahrostami, A. Patel, and J. K. Nørskov, Understanding catalytic activity trends in the oxygen reduction reaction, Chem. Rev. **118**, 2302 (2018).

[75] F. Calle-Vallejo, J. I. Martínez, J. M. García-Lastra, E. Abad, and M. T. M. Koper, Oxygen reduction and evolution at single-metal active sites: Comparison between functionalized graphitic materials and protoporphyrins, Surf. Sci. **607**, 47 (2013).

[76] K. Mathew, R. Sundararaman, K. Letchworthweaver, T. A. Arias, and R. G. Hennig, Implicit solvation model for density-functional study of nanocrystal surfaces and reaction pathways, J. Chem. Phys. **140**, 084106 (2014).

[77] H. Xu, D. Cheng, D. Cao, and X. C. Zeng, A universal principle for a rational design of single-atom electrocatalysts, Nat. Catal. **1**, 339 (2018).

[78] S. Li, G. S. Frankel, and C. D. Taylor, Theoretical relations between electronic and ionic work functions, standard reduction potentials for metal dissolution and the corrosion potential, J. Electrochem. Soc. **169**, 081506 (2022).

[79] L. B. Skinner, C. Huang, D. Schlesinger, L. G. M. Pettersson, A. Nilsson, and C. J. Benmore, Benchmark oxygen-oxygen pair-distribution function of ambient water from x-ray diffraction measurements with a wide Q-range, J. Chem. Phys. **138**, 074506 (2013).

[80] M. J. Gillan, D. Alfè, and A. Michaelides, Perspective how good is DFT for water?, J. Chem. Phys. **144**, 130901 (2016).

[81] W. L. Scopel, F. Crasto de Lima, P. H. Souza, J. E. Padilha, and R. H. Miwa, Bridging borophene and metal surfaces: Structural, electronic, and electron transport properties, J. Phys. Chem. C **127**, 17556 (2023).

[82] N. Mounet, M. Gibertini, P. Schwaller, D. Campi, A. Merkys, A. Marrazzo, T. Sohier, I. E. Castelli, A. Cepellotti, and G. Pizzi, *et al.*, Two-dimensional materials from high-throughput computational exfoliation of experimentally known compounds, Nat. Nanotechnol. **13**, 246 (2018).